Supplementary Information for: Source Mineralogy and Transport History Shape the Compositional Heterogeneity of Long-Range Transported Saharan Dust

Julian Weng[1], Yufang Hao[1], Benjamin T. Brem[1], Tianqu Cui[1], Sophie Darfeuil[2], Gaëlle Uzu[2], Jean-Luc Jaffrezo[2], Martin Steinbacher[3], Martine Collaud Coen[4], Thaleia Gkraikou[5], Konstantina Oikonomou[5], Jean Sciare[5], Claudia Mohr[1,6], Andre S. H. Prévôt[1], Martin Gysel-Beer[1], Imad El Haddad[1], and Patrik Winiger[1]

[1]PSI Center for Energy and Environmental Sciences, 5232 Villigen PSI, Switzerland
[2]Université Grenoble Alpes, CNRS, INRAE, IRD, Grenoble-INP, IGE, 38000 Grenoble, France
[3]Swiss Federal Laboratories for Materials Science and Technology, Empa, 8600 Dübendorf, Switzerland
[4]Federal Office of Meteorology and Climatology, MeteoSwiss, 1530 Payerne, Switzerland
[5]Climate and Atmosphere Research Center, The Cyprus Institute, Nicosia, 2121, Cyprus
[6]Department of Environmental Systems Science, ETH Zurich, 8092 Zürich, Switzerland

Correspondence: Patrik Winiger (patrik.winiger@psi.ch)

Contents

S1 Detection of Saharan dust events at the JFJ by aerosol optical properties **4**

S2 Sample selection strategy **5**

S2.1 Saharan dust event samples 5

S2.2 *Non-Dust* reference samples 7

S2.3 Filtering of Saharan dust influenced samples from the *Non-Dust* reference time series 7

S3 Quantification of planetary boundary layer intrusions to the JFJ **9**

S4 Chemical analysis of filter samples: sample preparation and measurement specifications **9**

S4.1 Metal and trace element composition 9

S4.2 Major inorganic anions and cations 12

S4.3 Bulk water soluble organic carbon 12

S5 Mass reconstruction of PM_{10} under long-range transported Saharan dust conditions at the JFJ **13**

S5.1 Anions 13

S5.1.1 Inorganic nitrates and sulfates 13

S5.1.2 Carbonates 17

S5.1.3 Oxides 19

S5.2 Crustal elements and trace elements 19

S5.3 Water soluble organic matter 19

S5.4 Mass balance with gravimetric PM_{10} 22

S6 Obtainment of dust plume source regions and transport parameters from remote sensing satellite observation **24**

S6.1 Data origins, processing and visualization 24

S6.2 Uncertainties associated with parameter obtainment and validation with independent *in-situ* observations . . 24

S6.3 An example case of satellite remote sensing and reanalysis model products for the Saharan dust plume observed at the JFJ on 2021-04-02 26

S7 Comparison of *Dust* and *Non-Dust* element mass concentrations at the JFJ **27**

S7.1 Data coverage above limits of quantification 27

S7.2 Median element mass concentrations and enhancements in *Dust* samples 29

S7.3 Statistical testing of composition under *Dust*-conditions in comparison with *Non-Dust*-conditions 31

S8 Variability of water-soluble ion composition within the *Dust* samples **32**

S9 Compositional heterogeneity of *Dust* driven by source regions and transport time 33

S10 Statistical testing of *Dust* composition variability driven by source regions 34

S11 Statistical testing of *Dust* composition variability driven by transport time 36

S12 Allocation of *Dust* composition variability to different Saharan dust plume source regions 38

S13 Impact of transport time on *Dust* composition 41

S14 Overview of instruments and methods applied in this study 43

S1 Detection of Saharan dust events at the JFJ by aerosol optical properties

Saharan dust influence was detected online *in-situ* based on the change of the wavelength dependence (i.e. the Ångström exponent) of the single scattering albedo (SSA) during dust events (Collaud Coen et al., 2004, 2026). In short, the comparatively larger particle size and distinct chemical composition of mineral dust results in a negative Ångström exponent. In that way, binary dust flags (*Dust* or *Non-Dust*) can be obtained.

From online wavelength-resolved aerosol scattering and absorption measurements at the JFJ, the Ångström exponent of the SSA was calculated with an hourly temporal resolution. Aerosol scattering coefficients at three wavelengths ($450\,\mathrm{nm}$, $550\,\mathrm{nm}$, $700\,\mathrm{nm}$) were measured with an integrating nephelometer (model 3563, TSI Inc., USA). Aerosol absorption coefficients at seven wavelengths ($370\,\mathrm{nm}$, $470\,\mathrm{nm}$, $520\,\mathrm{nm}$, $590\,\mathrm{nm}$, $660\,\mathrm{nm}$, $880\,\mathrm{nm}$, $950\,\mathrm{nm}$) were derived from aethalometers (AE-31, Magee Scientific, Slovenia, for the period 2011–2015; AE-33, Magee Scientific, Slovenia, for the period 2015–2021). The binary optical dust flags do not allow direct quantification of the strength of a Saharan dust event.

S2 Sample selection strategy

S2.1 Saharan dust event samples

Table S1. List of Saharan dust events analyzed as *Dust* samples in this study. Event numbers are denoted with -A and -B for cases where dust plumes were detected on consecutive days at the JFJ, but online PM_{10} data, satellite remote sensing data and chemical observations indicate separate plume events. Full plume periods were retrieved from online optical flags as well as online *in-situ* PM_{10} data and are provided for the first day of each separate plume event.

HiVol filter sampling date	Event number (analysis ID)	Gravimetric PM_{10} [µg/m^3]	Full plume period
2011-04-10	1	25.3	2011-04-10 09:00 – 2011-04-12 03:00
2011-08-22	2	24.4	2011-08-20 22:00 – 2011-08-23 06:00
2011-09-03	3	21.6	2011-09-03 05:00 – 2011-09-03 19:00
2012-06-29	4	35.8	2012-06-28 13:00 – 2012-07-02 05:00
2012-06-30	4	29.1	
2012-07-01	4	24.0	
2012-07-27	5-A	26.8	2012-07-27 13:00 – 2012-07-28 15:00
2012-07-28	5-B	18.3	
2012-08-19	6	17.5	2012-08-19 03:00 – 2012-08-24 12:00
2012-08-20	6	21.1	
2012-08-21	6	35.2	
2012-08-22	6	19.9	
2012-08-23	6	20.3	
2013-08-03	7	36.0	2013-08-02 19:00 – 2013-08-05 05:00
2013-08-04	7	22.2	
2014-02-18	8-A	32.6	2014-02-18 04:00 – 2014-02-19 15:00
2014-02-19	8-B	31.7	
2014-04-03	9	20.6	2014-04-02 23:00 – 2014-04-03 11:00
2014-06-08	10	24.8	2014-06-07 16:00 – 2014-06-10 09:00
2014-06-09	10	18.4	

Table S1. Continued.

HiVol filter sampling date	Event number (analysis ID)	Gravimetric PM_{10} [µg/m^3]	Full plume period
2015-07-03	11	29.0	No online data available
2015-07-04	11	25.9	
2015-07-05	11	25.0	
2015-07-06	11	19.0	
2015-07-07	11	19.2	
2016-07-21	12	21.2	2016-07-21 05:00 – 2016-07-22 04:00
2017-03-12	13	18.8	2017-03-11 05:00 – 2017-03-13 07:00
2017-08-03	14	23.4	2017-08-02 18:00 – 2017-08-04 00:00
2018-04-08	15	25.0	2018-04-07 08:00 – 2018-04-08 16:00
2018-05-26	16	31.3	2018-05-25 23:00 – 2018-05-28 23:00
2019-06-25	17	33.4	2019-06-24 23:00 – 2019-06-27 09:00
2019-06-26	17	28.7	
2019-06-27	17	18.6	
2019-09-16	18	39.4	2019-09-15 17:00 – 2019-09-17 10:00
2020-01-24	19	31.5	2020-01-22 13:00 – 2020-01-26 09:00
2020-01-25	19	20.8	
2020-07-10	20	19.2	2020-07-10 02:00 – 2020-07-10 23:00
2021-02-06	25	147	2021-02-06 01:00 – 2021-02-06 21:00
2021-02-22	21-A	33.4	2021-02-22 05:00 – 2021-02-25 09:00
2021-02-23	21-A	48.7	
2021-02-24	21-A	19.0	
2021-02-26	21-B	37.1	2021-02-25 22:00 – 2021-02-28 07:00
2021-02-27	21-B	24.2	
2021-03-03	22	61.5	2021-03-02 17:00 – 2021-03-05 05:00
2021-03-04	22	58.7	
2021-04-02	23	40.3	2021-04-02 00:00 – 2021-04-03 10:00
2021-08-13	24	21.8	2021-08-13 05:00 – 2021-08-16 03:00

S2.2 *Non-Dust* reference samples

A statistical justification of the composite sample selection scheme, including comparison with full time periods can be found in Weng et al. (2026).

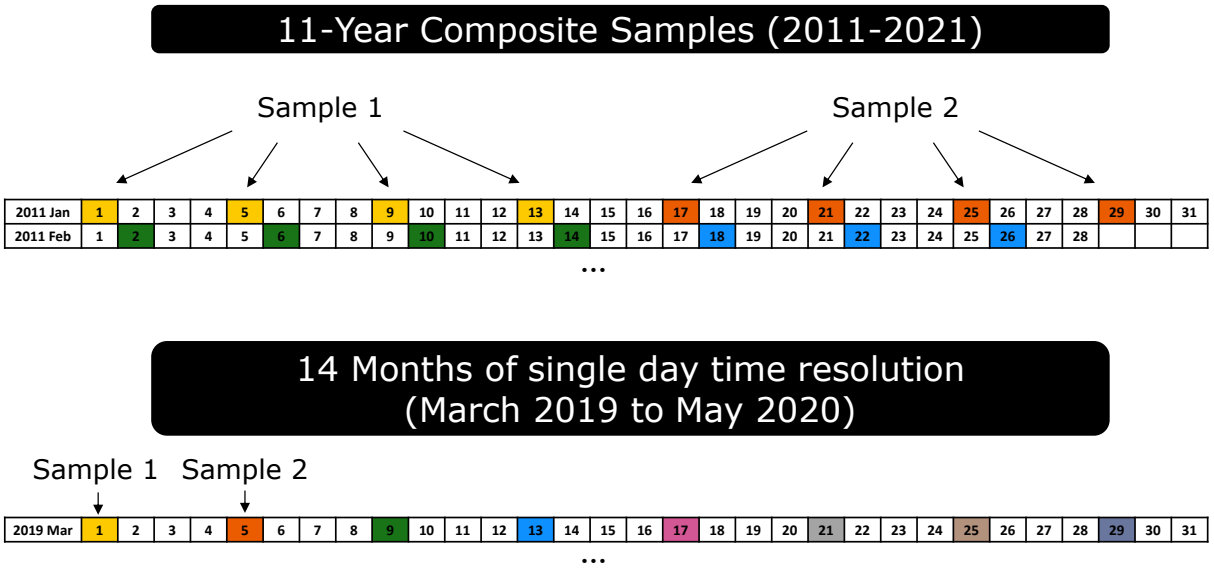


Figure S1. Schematic of filter selection and pooling strategy for *Non-Dust* samples. The 11-year composite samples are displayed at the top, 14-month daily time resolution samples at the bottom.

S2.3 Filtering of Saharan dust influenced samples from the *Non-Dust* reference time series

The detection of Saharan dust events by the aerosol optical *in-situ* method (Sect. S1) offers a reliable, yet non-quantitative approach. Therefore, for filtering of the reference time series for samples with considerable Saharan dust influence, a quantitative threshold based on titanium (Ti) ambient concentrations was applied, in coordination with the optical flags. Ti was selected due to strong enhancement under Saharan dust conditions over background *Non-Dust* concentrations at the JFJ (Sect. S7.3), as well as complete data coverage above limits of quantification for *Non-Dust* samples (Table S4).

A detailed description of Saharan dust filtering for the 11-year composite sample time series can be found in Weng et al. (2026). A Ti-threshold of $0.002\,\mu g\,m^{-3}$ was applied for these samples, which were extracted by a soft digestion (without hydrofluoric acid, HF) before analysis by Inductively Coupled Plasma Mass Spectrometry (ICP-MS, cf. Sect. S4.1).

The 14-month daily time resolution samples were extracted by a harsh digestion (with HF, Sect. S4.1), and accordingly, a different Ti-threshold of $0.018\,\mu g\,m^{-3}$ was applied. This threshold was defined based on comparison with optical Saharan dust flags (Fig. S2). A tradeoff was established by retaining locally influenced dust transport to the JFJ (through planetary boundary layer intrusions, PBLi), yet removing peak long-range transported Saharan dust events.

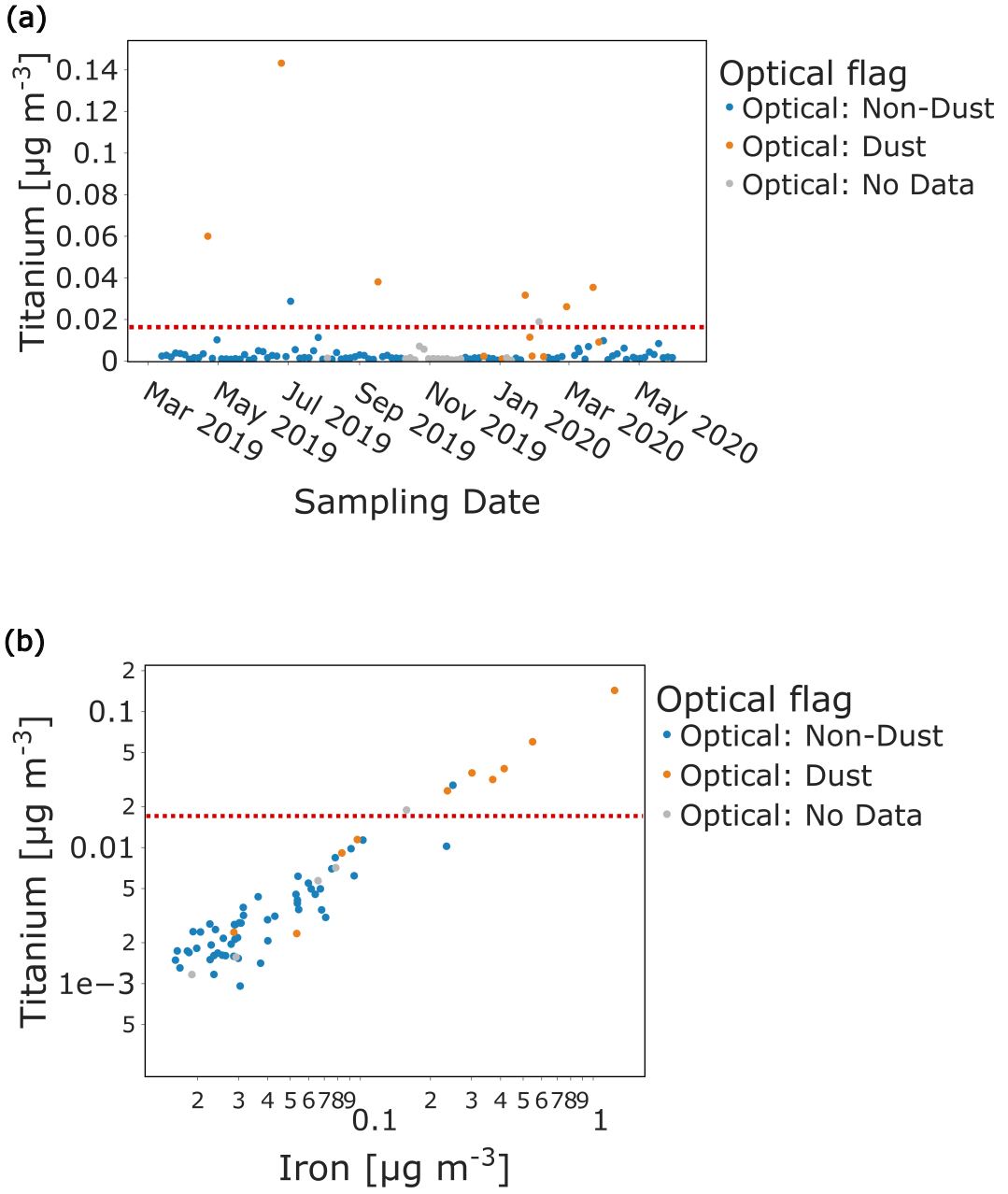


Figure S2. (a) Ti mass concentration time series for the 14-month daily time resolution samples. Sample markers are colored by optical flags, where *Dust* (orange) means at least a consecutive 12 h period of positive optical flag overlapping with the sampling time. (b) Ti mass concentrations as a function of Fe mass concentrations for the same samples, also colored according to optical Saharan dust flags. In both plots, the Saharan dust filtering threshold of $0.018\,\mu g\,m^{-3}$ Ti is indicated as a dashed red line.

S3 Quantification of planetary boundary layer intrusions to the JFJ

The presence of polluted air masses from regional PBLi to the JFJ can be quantified by a range of tracer proxies (Herrmann et al., 2015). These PBLi tracers are characterized by intense, constant emission sources in the PBL and a well-constrained short atmospheric lifetime following their release.

For this study, NO_y/CO, measured online *in-situ* at the JFJ, was selected for use as a quantitative tracer for PBLi strength, as it exhibits no systematic bias even under strong *Dust* conditions (Weng et al., in preparation).

Carbon monoxide (CO) has been detected using nondispersive infrared absorption spectroscopy (APMA-360 and APMA-370, Horiba, Japan) before 2012. Since 2012, cavity ring-down spectroscopy (G2401, Picarro, USA) was applied. The sum of reactive nitrogen species NO_y includes NO and NO_2, peroxyacetyl nitrate, nitric acid (HNO_3), and particulate nitrate (Zellweger et al., 2000). It was measured by a chemiluminescence detector (CLD 89p, Eco Physics, Switzerland) after conversion of all NO_y species to NO on a heated gold catalyst ($300\,^{\circ}\mathrm{C}$) with $2\,\%$ CO as reducing agent (Zellweger et al., 1999, 2000).

S4 Chemical analysis of filter samples: sample preparation and measurement specifications

S4.1 Metal and trace element composition

Major elements and trace metals were measured by ICP-MS.

Two different digestion methods were applied depending on sample types. Either a harsh full mineralization with complete digestion of all elements but comparably high liability towards contamination on filter punches. Or a milder digestion with lower completeness (no full digestion of the filter punches) but minimization of filter matrix effects. The harsh digestion was applied on all *Dust* samples and on the 14 months one-day-resolution *Non-Dust* samples. The mild digestion was applied on all *Non-Dust* 11-year composite samples (relevant here only for *Ti*-based Saharan dust filtering, Sect. S2.3).

Full mineralization of $6.2\,\mathrm{cm}^3$ quartz filter punches was performed using ultra-trace metal grade concentrated acids ($6\,\mathrm{mL}$ of 69% HNO_3, $3\,\mathrm{mL}$ of 37% HCl, and 5 drops of 30% HF) in a $22\,\mathrm{mL}$ pre-cleaned teflon digestion vessel (Savillex, USA). The digestion vessel was maintained in a sealed state for $24\,\mathrm{h}$ on a hot plate at $140\,^{\circ}\mathrm{C}$. Subsequently, 10 drops of concentrated H_2O_2 were added to each sample, followed by complete evaporation at $68\,^{\circ}\mathrm{C}$. The resulting residues were then dissolved and quantitatively transferred into metal-free tubes containing 2% HNO_3.

Mild mineralization of $6.2\,\mathrm{cm}^3$ quartz filter punches was performed using ultra-trace metal grade concentrated acids without HF ($6\,\mathrm{mL}$ of 69% HNO_3, $3\,\mathrm{mL}$ of 37% HCl, and 10 drops of concentrated H_2O_2) in a $22\,\mathrm{mL}$ pre-cleaned teflon digestion vessel (Savillex, USA). The digestion vessel was kept sealed for $24\,\mathrm{h}$ on a hot plate at $140\,^{\circ}\mathrm{C}$. After complete evaporation at $68\,^{\circ}\mathrm{C}$, samples were dissolved and transferred into metal free tubes with 2% HNO_3.

Measurement of about 45 elements was carried out using a triple quadrupole ICP-MS (iCAP TQ ICP-MS, Thermo Fisher Scientific, USA), coupled with an autosampler (SC4 DX, Elemental Scientific, USA) and FAST valve introduction. The analytical mode (SQ, or TQ-He / TQ-O2 / TQ-NH3) applied to each element was selected on the basis of the *Thermo Fisher Scientific library and matrix advice* plus additional tests of interferences. Quantification was performed using external calibration and

isotope dilution. Mineralization yields, analytical reproducibility, and accuracy were evaluated using certified reference materials (ERM-CZ120 fine dust and BCR-723 road dust, European Commission Joint Research Centre, Belgium), in-house mixed standard solutions, and certified stock solutions (CMS-5 and IV-STOCK50, Analab, France), respectively. Empirical mineralization yields (Table S2) were then used to correct for obtained element mass concentrations. Procedural and instrumental uncertainties were below 10% for the elements.

Fieldblank subtraction and calculation of ambient mass concentrations from water extract values were carried out as described in Sect. S4.3.

Table S2. Recovery rates [%] for elements after full digestion, obtained from analysis of the certified reference materials ERM-CZ120 fine dust and BCR-723 road dust.

Element	Recovery [%]
Na	90
Mg	89
Al	87
K	91
Ca	89
Sc	75
Ti	79
V	88
Cr	76
Mn	88
Fe	86
Co	91
Ni	105
Cu	82
Zn	96
Ga	85
Rb	87
Sr	86
Y	98
Zr	34
Cd	69
Cs	68
Ba	97
La	90
Ce	92
Sm	83
Tb	58
Pb	95
Th	77
U	68

S4.2 Major inorganic anions and cations

Consistent with previously established standard protocols (Jaffrezo et al., 1998; Waked et al., 2014), a suite of inorganic anions and cations was quantified using Ion Chromatography Mass Spectrometry (IC–MS). IC–MS was applied for *Dust* samples and the *Non-Dust* 11-year composite samples.

In brief, for each sample, four circular filter punches ($18\,\mathrm{mm}$ diameter) were submerged in $6\,\mathrm{mL}$ of Milli-Q® and subjected to vortex mixing for $20\,\mathrm{min}$. The resulting extracts were subsequently passed through Milli-Q® -preconditioned IC syringe filters ($0.2\,\mu\mathrm{m}$ pore size, Acrodisc, Cytiva, USA) and directly injected into the IC-MS. Further details on material and sample preparation are provided in Weng et al. (2026).

For detection of cations, an IC setup (INTEGRION, Thermo Fisher Scientific, USA) was used, configured with isocratic methanesulfonic acid (MSA) eluent and CG16-$4\,\mu\mathrm{m}$/CS16-$4\,\mu\mathrm{m}$ columns ($2\,\mathrm{mm}$, Thermo Fisher Scientific, USA). For anions, a coupled IC-MS (INTEGRION and ISQ EC, Thermo Fisher Scientific, USA) was used configured with gradient KOH eluent and AG11HC-$4\,\mu\mathrm{m}$/AS11HC-$4\,\mu\mathrm{m}$ columns (2mm, Thermo Fisher Scientific, USA). The mass spectrometer was run in negative electrospray mode (–2700 V). Procedural and analytical uncertainties did not exceed 10% for either method. Limits of detection for most analytes were below the $\mathrm{ng\,mL^{-1}}$ threshold in the analyzed samples.

Fieldblank subtraction and calculation of ambient mass concentrations from water extract values were carried out as described in Sect. S4.3.

S4.3 Bulk water soluble organic carbon

The water extraction procedure is described in detail in Weng et al. (2026). In short, 4 and 8 filter punches ($\varnothing\ 14\,\mathrm{mm}$) were submerged in $12\,\mathrm{mL}$ of ultrapure water (Milli-Q®, $18.2\,\mathrm{M\Omega\,cm}$ at $25\,^{\circ}\mathrm{C}$, total organic carbon $< 5\,\mathrm{ppb}$, Merck Millipore, Germany) for *Dust* and *Non-Dust* samples, respectively. The lower number of filter punches for *Dust* samples assured measurements in a comparable concentration range, besides an economical use of filter material. This was followed by sonication ($30\,^{\circ}\mathrm{C}$ for $20\,\mathrm{min}$), vortexing ($1\,\mathrm{min}$) and filtration (nylon membrane filters, $0.45\,\mu\mathrm{m}$ pore size, HPLC syringe filters YETI, Infochroma AG, Switzerland).

Aliquots of the extracts were analyzed for their total organic carbon (TOC) content by a TOC analyzer (TOC-L-series, Shimadzu, Japan). The TOC analyzer was operated in the non-purgeable organic carbon (NPOC) protocol. The NPOC protocol features removal of the inorganic carbon fraction by acidification (HCl, H_3PO_4) and sparging of water extracts before measurement (Cui et al., 2024). In that way, correct quantification of bulk aerosol water soluble organic carbon (WSOC) is assured also for Saharan dust samples that can contain high levels of inorganic carbon (e.g. calcite or dolomite minerals).

Sample water extract TOC concentrations were subtracted by respecitive fieldblank values. Then, from water extract TOC concentrations, quantification of ambient WSOC mass concentrations ρ_{WSOC} in $\mu\mathrm{g\,m^{-3}}$ was achieved using the following relationship:

$$\rho_{WSOC} = \frac{\rho_{TOC\ extract}(i) * V_{extraction}}{f_{filter}} * \frac{1}{V_{sampled\ air}} \tag{S1}$$

With the water extract TOC concentrations $\rho_{TOC\ extract}$ [$\mu g\,mL^{-1}$], extraction volumes $V_{extraction}$ [mL], fraction of extracted filter area of total filter area f_{filter}

$$f_{filter} = \frac{punch\ area * number\ of\ punches}{effectively\ sampled\ filter\ area} \tag{S2}$$

and sampled air volume $V_{sampled\ air}$ [m^3]

$$V_{sampled\ air} = sampling\ duration\ [h] * sampling\ rate\ [m^3 h^{-1}] \tag{S3}$$

S5 Mass reconstruction of PM_{10} under long-range transported Saharan dust conditions at the JFJ

S5.1 Anions

S5.1.1 Inorganic nitrates and sulfates

Under *Non-Dust* conditions at the JFJ, mass concentrations of the major aerosol inorganic ions — sulfate, nitrate and ammonium — are strongly bound to pollution transport through PBLi (Fröhlich et al., 2015). Sulfate and *filter-based* nitrate [1] is well saturated by ammonium (cf. blue markers in Fig. S3, simple linear regression $SLR:\ NH_{4\ if\ neutralized}^{+} = 0.83 * NH_{4\ observed}^{+} + 0.019$, $R^2 = 0.92$). Under *Dust* conditions, substantial parts of nitrate and sulfate are bound to metal cations, either from minerals in the source regions (e.g. evaporites) (Rodríguez et al., 2011) or through oxidation of precursor gases on dust and anion exchange (Usher et al., 2003). Accordingly, nitrate and sulfate are not neutralized by ammonium under *Dust* conditions (cf. orange markers in Fig. S3).

For estimation of the fractions of non-ammonium-sulfate (NAS) and non-ammonium-nitrate (NAN) under *Dust* conditions, the following approach was applied: In agreement with previous studies (Rodríguez et al., 2011), no substantial amounts of ammonium are carried by Saharan dust, which could be a consequence of transfer reactions of anions to metal cations (Fig. S4). Accordingly, under *Dust*-conditions, measured ammonium mass concentrations agree well with PBLi strength at the JFJ (Fig. S5) and it can be assumed that ammonium originates mostly from regional PBLi. The mass concentrations of ammonium sulfate and filter-based ammonium nitrate under *Dust* conditions are therefore likely dominated by regional PBLi and were estimated from measured ammonium mass concentrations. For this, an empirical molar concentration ratio R_n of ammonium sulfate and filter-based ammonium nitrate at the JFJ was estimated based on the median R_n observations of all *Non-Dust* samples.

$$R_n = \frac{c_n(\mathrm{SO_4^{2-}})}{c_n(\mathrm{NO_3^-})} = 2.61\ (empirical) \tag{S4}$$

[1] Filter based quantification of nitrate from ammonium nitrate is subject to biases from evaporative losses (Chow et al., 2005). Therefore, nitrate quantified from HiVol filters under *Non-Dust*-conditions is called *filter-based* nitrate here and not considered as a quantitative estimate.

Then, the following steps lead to ammonium bound sulfate ($c_m(\mathrm{SO_4^{2-}})$) and ammonium bound *filter-based* nitrate ($c_m(\mathrm{NO_3^-})$) mass concentrations.

$$c_n(\mathrm{NH_4^+}) = 2\,c_n(\mathrm{SO_4^{2-}}) + c_n(\mathrm{NO_3^-}) \tag{S5}$$

$$\rightarrow c_n(\mathrm{NH_4^+}) = 2\,c_n(\mathrm{SO_4^{2-}}) + \frac{c_n(\mathrm{SO_4^{2-}})}{R} = \left(2 + \frac{1}{R_n}\right) c_n(\mathrm{SO_4^{2-}}) \tag{S6}$$

$$\rightarrow c_n(\mathrm{SO_4^{2-}}) = \frac{1}{\left(2 + \frac{1}{R_n}\right)}\, c_n(\mathrm{NH_4^+}) \tag{S7}$$

$$\rightarrow c_m(\mathrm{SO_4^{2-}}) = \frac{1}{\left(2 + \frac{1}{R_n}\right)}\, c_m(\mathrm{NH_4^+})\, \frac{M(\mathrm{SO_4^{2-}})}{M(\mathrm{NH_4^+})} \tag{S8}$$

$$and\ likewise: c_m(\mathrm{NO_3^-}) = \frac{1}{(2R+1)}\, c_m(\mathrm{NH_4^+})\, \frac{M(\mathrm{NO_3^-})}{M(\mathrm{NH_4^+})} \tag{S9}$$

with the molar concentrations c_n and molar masses M of sulfate ($M = 96.06\,\mathrm{g\,mol^{-1}}$), nitrate ($M = 62.01\,\mathrm{g\,mol^{-1}}$) and ammonium ($M = 18.04\,\mathrm{g\,mol^{-1}}$).

With $c_m(\mathrm{SO_4^{2-}})$ and $c_m(\mathrm{NO_3^-})$, NAS and NAN mass concentrations under *Dust*-conditions can be calculated as the difference from total measured sulfate and *filter-based* nitrate.

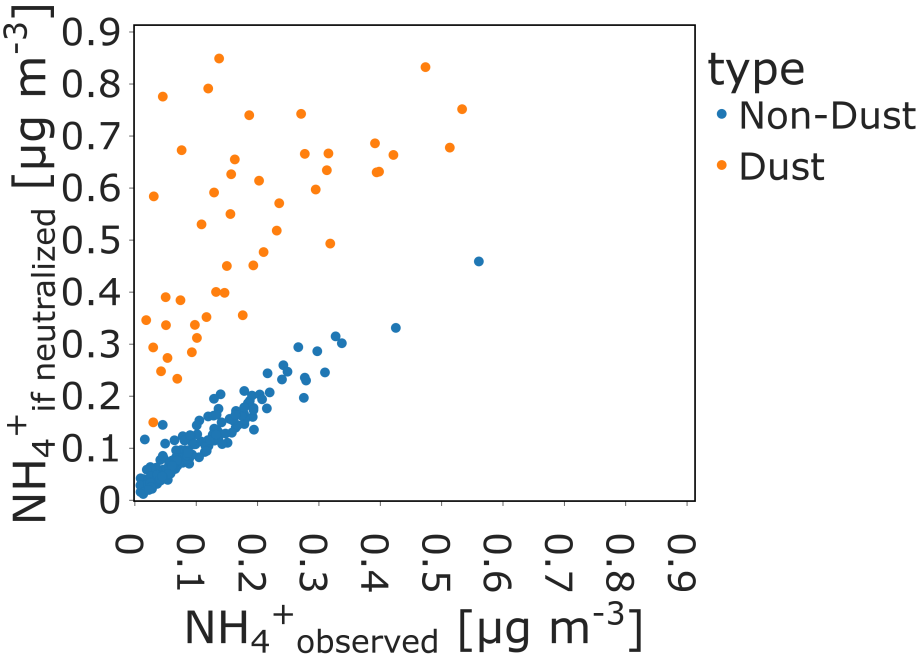


Figure S3. For *Non-Dust* and *Dust* samples, comparison of measured ammonium mass concentrations ($NH^+_{4\ observed}$, from IC-MS) and theoretical ammonium mass concentrations ($NH^+_{4\ if\ neutralized}$), calculated from ion balance with measured nitrate and sulfate (IC-MS) under the assumption of full neutralization. For clarity of visualization, one data point of *Dust* samples exceeding $1.2\,\mu g\,m^{-3}$ is not shown.

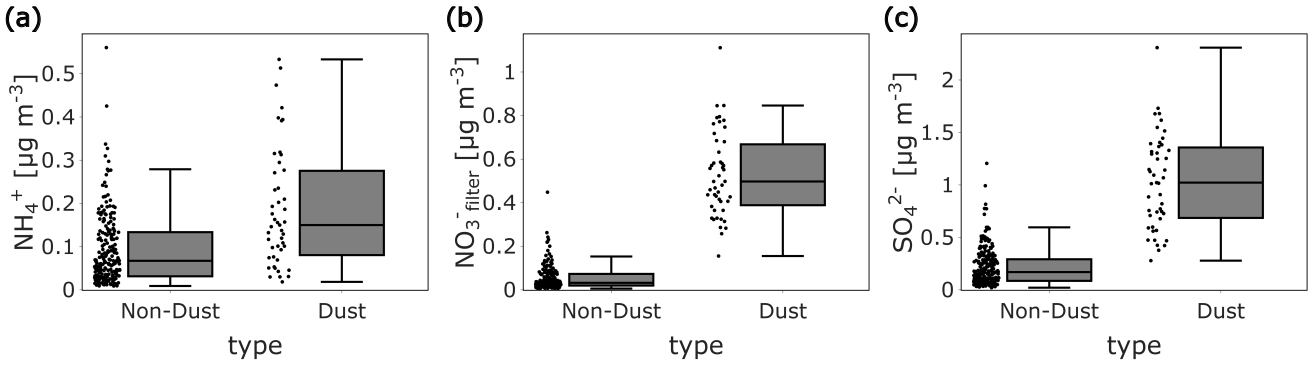


Figure S4. Box plots of mass concentrations of (a) ammonium, (b) filter-based nitrate and (c) sulfate under both *Non-Dust* and *Dust* conditions.

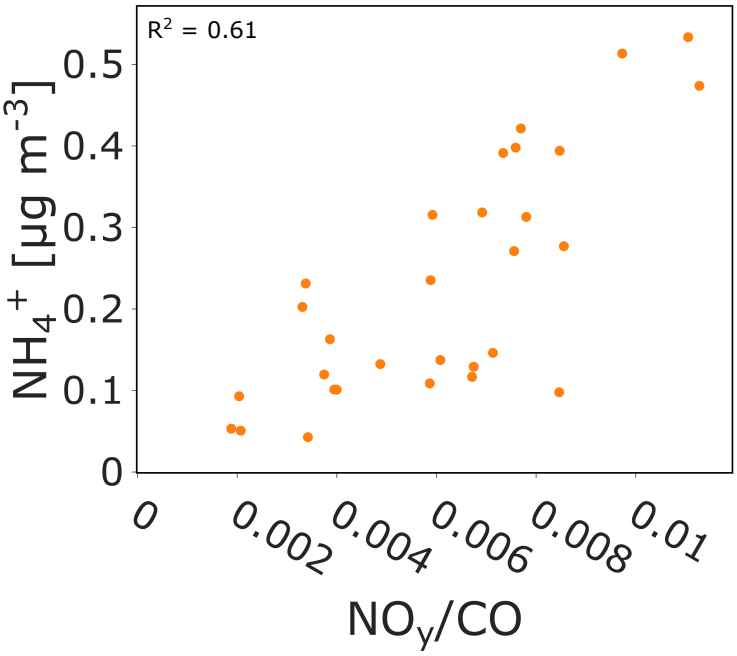


Figure S5. Measured ammonium mass concentrations of *Dust* samples as a function of the PBLi tracer NO_y/CO (details on NO_y/CO are provided in Sect. S3). The coefficient of determination R^2 is provided.

S5.1.2 Carbonates

Carbonate (CO_3^{2-}) mass concentrations were estimated from thermal–optical OC/EC measurements with the NIOSH protocol. The NIOSH protocol was developed to thermally separate the carbonate related inorganic carbon (IC) fraction from the majority of OC, which is evolving at lower temperatures or the pyrolysis step (Chow et al., 2001). Carbonates are known to evolve mainly in the OC4 ($850\,^{\circ}\mathrm{C}$) step of NIOSH. Accordingly, the ratio OC4/OC is substantially elevated for most *Dust* samples (median *Non-Dust*: $OC4/OC = 0.176$, median *Dust*: $OC4/OC = 0.244$, Fig. S6). Assuming that under *Non-Dust* conditions the abundance of carbonates is negligible compared to OC, the $OC4/OC$ ratio of *Non-Dust* in Fig. S6 makes clear that, besides carbonates, also organic compounds contribute to OC4. The fraction of OC4 remains however relatively constant in *Non-Dust* samples. Therefore, the IC contribution to OC for *Dust* samples can be estimated using the median OC4/OC value under *Non-Dust*-conditions:

$$IC/OC(Dust) = OC4/OC(Dust) - OC4/OC\ (median\ \textit{Non-Dust}) \tag{S10}$$

Carbonate mass concentrations $c_m(Carbonate)$ can then be calculated by:

$$c_m(Carbonate) = IC/OC * c_m(OC) * \frac{M(\mathrm{CO_3^{2-}})}{M(\mathrm{C})} \tag{S11}$$

with the molar masses of carbonate ($M = 60.01\,\mathrm{g\,mol^{-1}}$) and carbon ($M = 12.00\,\mathrm{g\,mol^{-1}}$).

The molar concentrations of obtained carbonate loadings correlate well with calcium from ICP-MS, its natural binding partner in mineral calcite ($R^2 = 0.98$, Fig. S7). However, calcium is about a factor two more abundant ($SLR\ slope = 2.2$). This can be related to the presence of other Ca minerals, carbonate depletion along the transport and underestimation of carbonate concentrations due to their contribution also to other fractions than OC4 in the NIOSH protocol.

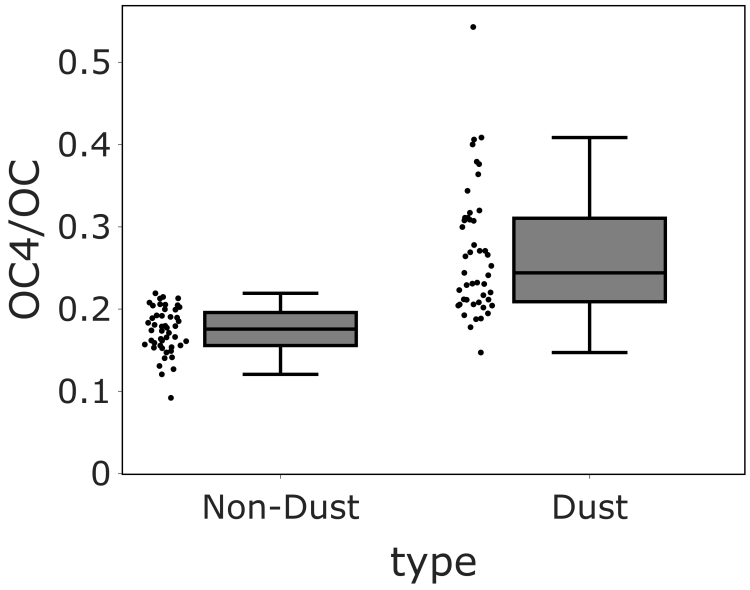


Figure S6. Box plot of the OC4/OC-ratio of thermal–optical OC/EC measurements with the NIOSH protocol for *Non-Dust* and *Dust* samples.

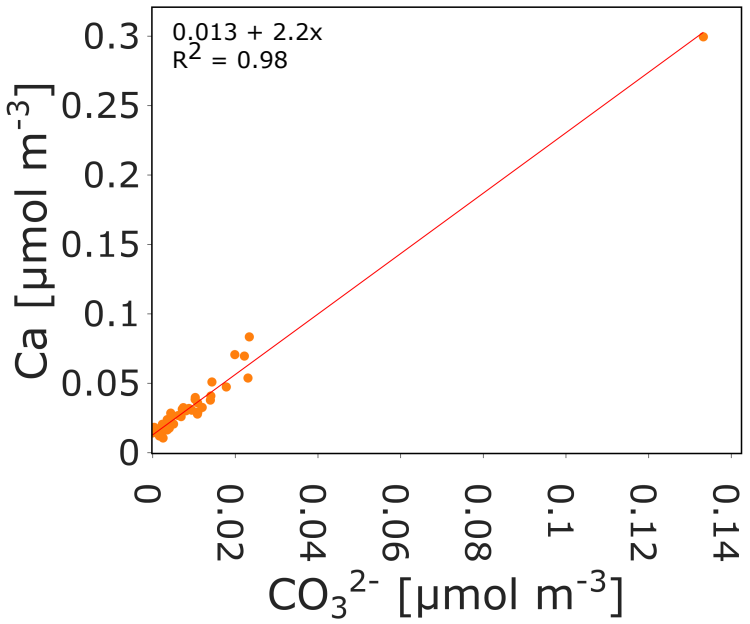


Figure S7. Obtained carbonate molar concentrations as a function of calcium molar concentrations (from ICP-MS measurements). A linear fit equation and coefficients of determination R^2 are provided.

S5.1.3 Oxides

Oxide (O^{2-}) as a binding partner of cations in minerals cannot be directly measured. Oxide mass concentrations are therefore calculated under consideration of the measured dominating inorganic anion — NAN, NAS, chloride and carbonate — and crustal element cation mass concentrations. All crustal element cations not bound to the dominating other anions were assumed to be neutralized by oxide. The crustal elements were considered to occur in their most common valence in natural minerals (White, 2020; Chow et al., 2015) (Table S3). Then, valence equivalents eq for each species i were calculated with the molar concentrations c_n (calculated from measured mass concentrations by ICP-MS with molar masses in Table S3) as:

$$eq(i) = valence(i) * c_n(i) \tag{S12}$$

The oxide equivalents needed for a valence balance and the oxide mass concentration c_m are then obtained with the molar concentration of oxide $M(oxide)$ =16.00 $\mathrm{g\,mol^{-1}}$ by:

$$eq(oxide) = \Sigma_i \; eq(i) \tag{S13}$$

$$c_m(oxide) = \frac{eq(oxide)}{2} * M(oxide) \tag{S14}$$

S5.2 Crustal elements and trace elements

Apart from Si, all crustal elements and trace metals were quantified by ICP-MS. Si cannot be reliably quantified, as the HiVol filters are composed of quartz (SiO_2). The Si/Al ratio however is known to be relatively stable throughout the whole Saharan desert region (Caquineau et al., 1998). Based on geological mineral (Caquineau et al., 1998) and also aerosol samples (Rodríguez et al., 2011), a constant $Si/Al = 2.1$ was assumed to estimate Si mass concentrations from Al mass concentrations.

S5.3 Water soluble organic matter

Unlike the thermal–optical OC, WSOC obtained from the TOC analyzer is not affected by inorganic carbon (carbonates). WSOC was therefore utilized as the best estimate for organic matter under *Dust*-conditions. WSOC was converted to water soluble organic aerosol (WSOA) using organic matter/organic carbon (OM/OC) ratios obtained from Offline-AMS measurements of *Non-Dust* filters (Weng et al., 2026). A median OM/OC of 2.31 was applied, considering that the OM/OC is relatively stable under different conditions at the JFJ (for $n = 206$ samples: median OM/OC = 2.3, IQR 2.2 to 2.4). At the JFJ, WSOA is a good estimate for total OA, as the OA water-solubility lies at around 83% (Weng et al., 2026).

Table S3. Valence and molar mass of crustal elements and inorganic anions used for calculation of oxide mass concentrations. Iron (Fe) valence represents an average of Fe^{2+} and Fe^{3+}, assuming they are present in equal abundance. For simplicity, element names are listed in their neutral form.

Element/Anion	Valence	Molar mass [g mol^{-1}]
Li	+1	6.94
Be	+2	9.0122
B	+3	10.81
Na	+1	22.99
Mg	+2	24.305
Al	+3	26.982
K	+1	39.098
Ca	+2	40.078
Sc	+3	44.956
Ti	+4	47.867
V	+5	50.942
Cr	+3	51.996
Mn	+2	54.938
Fe	+2.5	55.845
Co	+2	58.933
Ni	+2	58.693
Cu	+2	63.546
Zn	+2	65.38
Ga	+3	69.723
Ge	+4	72.630
Rb	+1	85.468
Sr	+2	87.62
Y	+3	88.906
Zr	+4	91.224
Mo	+6	95.95
Rh	+3	102.91
Cd	+2	112.41
Sn	+4	118.71
Cs	+1	132.91
Ba	+2	137.33

Table S3. Continued.

Element/Anion	Valence	Molar mass [g mol^{-1}]
La	+3	138.91
Ce	+4	140.12
Sm	+3	150.36
Tb	+3	158.93
Ho	+3	164.93
Pt	+2	195.08
Pb	+2	207.2
Bi	+3	208.98
Th	+4	232.04
U	+6	238.03
Si (estimated from Al)	+4	28.085
NAN-NO_3^-	-1	62.005
NAS-SO_4^{2-}	-2	96.06
Cl^-	-1	35.45
CO_3^{2-}	-2	60.008

S5.4 Mass balance with gravimetric PM_{10}

The reconstructed PM_{10} mass concentration under *Dust* conditions is defined by the following components:

$$PM_{10}\ (\text{Dust, reconstructed}) = NH_4NO_3\,(\text{filter}) + (NH_4)_2SO_4 + \text{NAN}\ (\text{NO}_3^-) + \text{NAS}\ (\text{SO}_4^{2-}) + CO_3^{2-} + Cl^- + O^{2-} + \text{crustal elements (Table S3)} + \text{WSOA} + \text{EC} \quad \text{(S15)}$$

Comparison of $PM_{10}\ (\text{Dust, reconstructed})$ with gravimetric PM_{10} shows a good correlation ($R^2 = 0.95$, Fig. S8). The mass recovery ratio, defined by $\frac{PM_{10}\ (\text{Dust, reconstructed})}{PM_{10}\ (Dust,\ gravimetric)}$, lies slightly below a complete recovery of 1 ($median\ recovery = 0.83\ with\ IQR = 0.77\ to\ 0.88$, Fig. S9). Potential contributions to the slight underestimation are: (i) the presence of crystal water in minerals (especially the abundant clays and gypsum (Yan et al., 2016)) which cannot be accounted for in the mass reconstruction; (ii) condensation of water on the filter material during conditioning ($RH = 50\%$). Hüglin *et al.* have shown that, especially for high inorganic component content, condensed water can contribute up to 25% of PM_{10} filter mass (Hueglin et al., 2005).

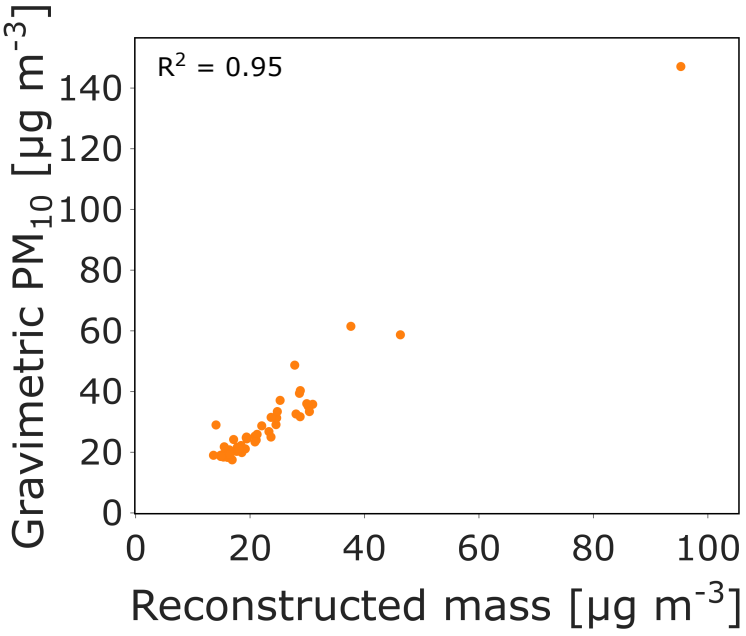


Figure S8. Comparison of reconstructed mass with the gravimetric PM_{10} of each *Dust* sample. The coefficient of determination R^2 is provided.

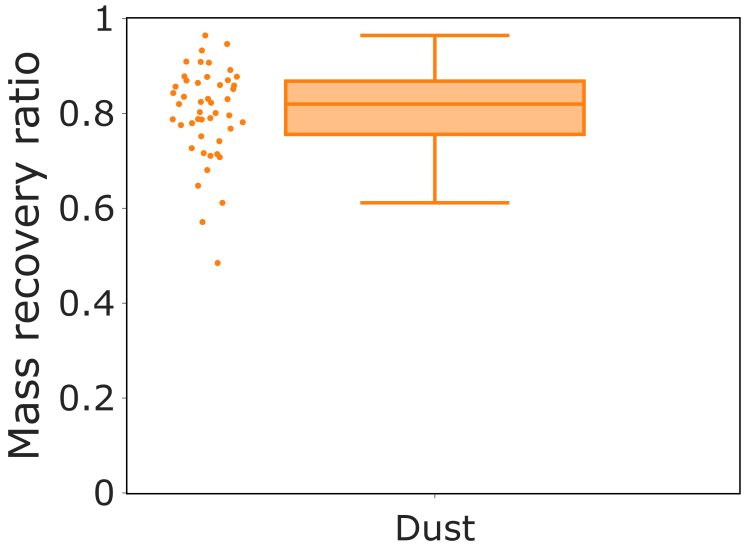


Figure S9. Box plot of the mass recovery ratio, i.e. the ratio of reconstructed mass to gravimetric PM_{10} for the *Dust* samples.

S6 Obtainment of dust plume source regions and transport parameters from remote sensing satellite observation

S6.1 Data origins, processing and visualization

Copernicus Atmosphere Monitoring Service (CAMS) European Centre for Medium-Range Weather Forecasts Atmospheric Composition Reanalysis 4 (EAC4) dust aerosol optical depth (AOD) at $550\,\mathrm{nm}$ was downloaded from https://doi.org/10.24381/d58bbf47 (Inness et al., 2019). National Aeronautics and Space Administration (NASA) Terra and Aqua Moderate Resolution Imaging Spectroradiometer (MODIS) AOD was obtained from https://doi.org/10.5067/MODIS/MOD08_D3.061 and https://doi.org/10.5067/MODIS/MYD08_D3.061. European Space Agency's (ESA) Meteosat Second Generation (MSG) Spinning Enhanced Visible and InfraRed Imager (SEVIRI) Dust RGB was downloaded from the EUMETSAT user portal, at https://user.eumetsat.int/catalogue/EO:EUM:DAT:MSG:DUST (last access: September 24, 2025) (Schmetz et al., 2002).

CAMS EAC4 dust AOD and MSG SEVIRI Dust RGB were retrieved programatically from the data stores, NASA Terra and Aqua MODIS AOD from the data store web interface. All data products were subsequently processed and visualized in Python (Python 3.10.9, Python Software Foundation, 2022, https://www.python.org/). For evaluation, data products were cut to adequate geospatial regions and consecutive satellite images were animated in .mp4 format.

S6.2 Uncertainties associated with parameter obtainment and validation with independent *in-situ* observations

Unambiguous allocation of dust plumes observed at JFJ to individual source emission events can be hampered by several factors: Increasing dilution along the transport and therefore reduction of dust plume associated AOD, observational interferences through cloud coverage and, for some cases, mixing of plumes of different origins in the Saharan Air Layer (which inherently exhibits high boundary layers with considerable dust loadings of different origins (Knippertz and Todd, 2012)). These factors impose uncertainties on some of the dust plume parameters presented in Fig. 1.

Apart from the geochemical fingerprints presented in this study, allocation of source regions and transport times are independently confirmed by size resolved *in-situ* PM measurements at the JFJ. A strong correlation ($R^2 = 0.51$) of $PM_{2.5}$/PM_{10}-ratios from online fine dust monitor (FIDAS 200, PALAS, Germany) measurements with plume transport times is found (Fig. S10). This is consistent with increased gravitational settling of more coarse particles with higher transport times (i.e. atmospheric age).

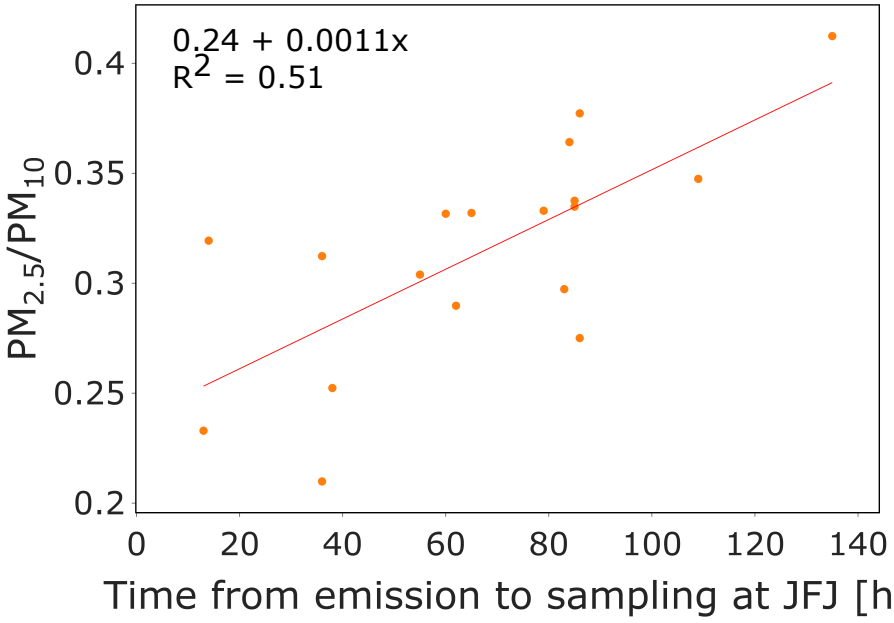


Figure S10. FIDAS fine dust monitor $PM_{2.5}/PM_{10}$ as a function of satellite remote sensing obtained transport times of Saharan dust plumes from emission start to the JFJ. FIDAS data are available from 11/2016 and only the events after that are considered. Depicted are average values corresponding to the time periods of the *Dust* PM_{10} filter samples analyzed in this study. A linear fit equation and coefficients of determination R^2 are provided.

S6.3 An example case of satellite remote sensing and reanalysis model products for the Saharan dust plume observed at the JFJ on 2021-04-02

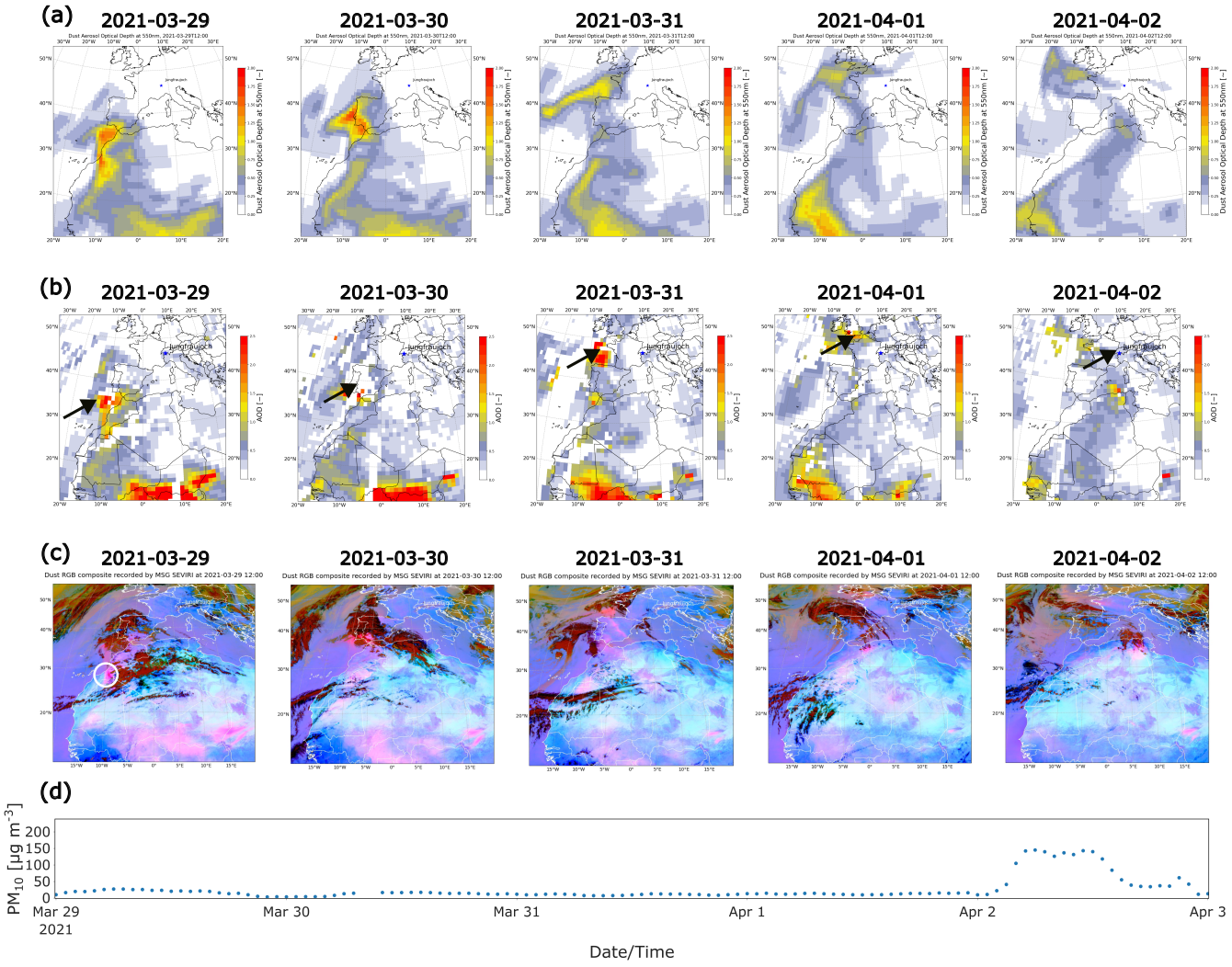


Figure S11. Overview of the different satellite remote sensing and reanalysis model products for the Saharan dust plume that reached the JFJ on 2021-04-02: (a) CAMS EAC4 dust AOD at 550 nm; (b) NASA Terra MODIS AOD; the black arrows indicated approximate plume positions on the trajectory from the emission source regions to the JFJ. (c) MSG SEVIRI Dust RGB; the white circle indicates the emission source region as constrained by the visual backtracking method of 15 min time-resolution satellite images. (d) For the same time period as satellite images, PM_{10} as measured online at the JFJ.

S7 Comparison of *Dust* and *Non-Dust* element mass concentrations at the JFJ

S7.1 Data coverage above limits of quantification

Data coverage of samples above limits of quantification was calculated for each element based on:

$$coverage[\%] = \frac{number\ of\ samples\ with\ values\ above\ limit\ of\ quantification}{total\ number\ of\ samples} \tag{S16}$$

Table S4. Data coverage [%] above limits of quantification of elements measured by ICP-MS for *Dust* and *Non-Dust* samples. *Non-Dust* samples are the 14-month daily time resolution samples (March 2019 to May 2020), which were analyzed using harsh filter digestion (with HF, just as *Dust* samples, Sect. S4.1.

Element	***Dust* [%]**	***Non-Dust* [%]**
Li	100.0	96.15
Be	100.0	10.58
B	57.45	14.42
Na	100.0	66.35
Mg	100.0	29.81
Al	100.0	22.12
K	100.0	38.46
Ca	100.0	95.19
Sc	100.0	61.54
Ti	100.0	100.0
V	100.0	93.27
Cr	72.34	3.85
Mn	100.0	55.77
Fe	100.0	57.69
Co	100.0	5.77
Ni	25.53	1.92
Cu	100.0	93.27
Zn	44.68	3.85
Ga	100.0	48.08
Ge	80.85	0.0

Table S4. Continued.

Element	***Dust* [%]**	***Non-Dust* [%]**
Rb	100.0	100.0
Sr	100.0	75.96
Y	61.7	0.96
Zr	76.6	0.96
Mo	48.94	0.96
Cd	100.0	81.73
Sn	95.74	29.81
Cs	100.0	68.27
Ba	91.49	0.96
La	100.0	31.73
Ce	100.0	16.35
Sm	97.87	1.92
Tb	59.57	0.96
Ho	70.21	0.96
Pb	100.0	97.12
Bi	100.0	83.65
Th	95.74	1.92
U	46.81	6.73
P	100.0	46.15
S	100.0	61.54
As	100.0	61.54
Se	100.0	96.15
Br	91.49	37.5
Sb	74.47	51.92

S7.2 Median element mass concentrations and enhancements in *Dust* samples

Table S5. Median mass concentrations of elements measured by ICP-MS for *Dust* and *Non-Dust* samples, and enrichment ratios (*Dust*/*Non-Dust*). Concentrations (and enrichment ratios) are only displayed for elements with $>10\,\%$ of data coverage (Table S4). ICP-MS recovery rates (Table S2) were not applied for the concentrations displayed, as enrichment ratios remain unaffected by this correction.

Element	***Dust*** **[μg m^{-3}]**	***Non-Dust*** **[μg m^{-3}]**	**Enrichment ratio**
Li	1.1e-03	2.9e-05	39
Be	5.7e-05		
B	3.9e-03		
Na	0.17	0.029	5.9
Mg	0.36	0.022	17
Al	1.6	0.15	11
K	0.43	0.032	14
Ca	0.93	0.050	19
Sc	3.0e-04	7.2e-06	42
Ti	0.095	0.0016	59
V	2.5e-03	6.3e-05	41
Cr	5.0e-03		
Mn	0.017	7.4e-04	23
Fe	0.87	0.031	28
Co	3.6e-04		
Ni	5.0e-03		
Cu	1.2e-03	4.3e-04	2.8
Zn	9.7e-03		
Ga	4.4e-04	2.9e-05	15
Ge	3.2e-04		
Rb	1.8e-03	6.6e-05	27
Sr	5.1e-03	3.7e-04	14
Y	6.5e-04		
Zr	2.9e-03		
Mo	0.010		
Cd	1.9e-05	4.6e-06	4.1
Sn	1.4e-04	1.1e-04	1.3

Table S5. Continued.

Element	*Dust* [μg m^{-3}]	*Non-Dust* [μg m^{-3}]	Enrichment ratio
Cs	1.0e-04	5.8e-06	17
Ba	9.9e-03		
La	9.3e-04	7.2e-05	13
Ce	1.9e-03		
Sm	1.6e-04		
Tb	2.4e-05		
Ho	2.4e-05		
Pb	1.3e-03	3.1e-04	4.1
Bi	1.5e-05	5.0e-06	3.0
Th	2.7e-04		
U	1.2e-04		
P	0.019	0.0018	11
S	0.42	0.084	5.1
As	2.6e-04	2.4e-05	11
Se	7.5e-05	1.1e-05	6.7
Br	1.0e-03	4.4e-04	2.4
Sb	1.0e-04	1.5e-04	0.67

S7.3 Statistical testing of composition under *Dust*-conditions in comparison with *Non-Dust*-conditions

Table S6. Two-sided Mann–Whitney *U* test p-values for the comparison of elements mass concentrations for *Dust* vs. *Non-Dust* samples. Species are displayed in ascending order according to their p-value. Only species with data coverage of at least 20 % in both categories (*Dust* and *Non-Dust*) were considered for testing (Table S4).

Element	Mann–Whitney *U* test p-value
Fe	8.6e-17
Na	1.8e-16
S	2.2e-16
Ti	1.0e-15
Al	1.4e-15
Pb	2.1e-14
Se	3.9e-14
Mn	1.4e-13
Ga	1.8e-13
Sr	4.1e-13
P	1.6e-12
As	3.9e-12
Sc	1.2e-11
Li	2.9e-11
V	3.9e-11
La	5.2e-11
K	5.9e-11
Mg	9.6e-11
Rb	1.0e-10
Cu	2.6e-10
Cs	4.4e-10
Cd	2.8e-09
Br	2.0e-08
Ca	2.7e-06
Sn	8.8e-03
Bi	9.8e-03
Sb	0.061

S8 Variability of water-soluble ion composition within the *Dust* samples

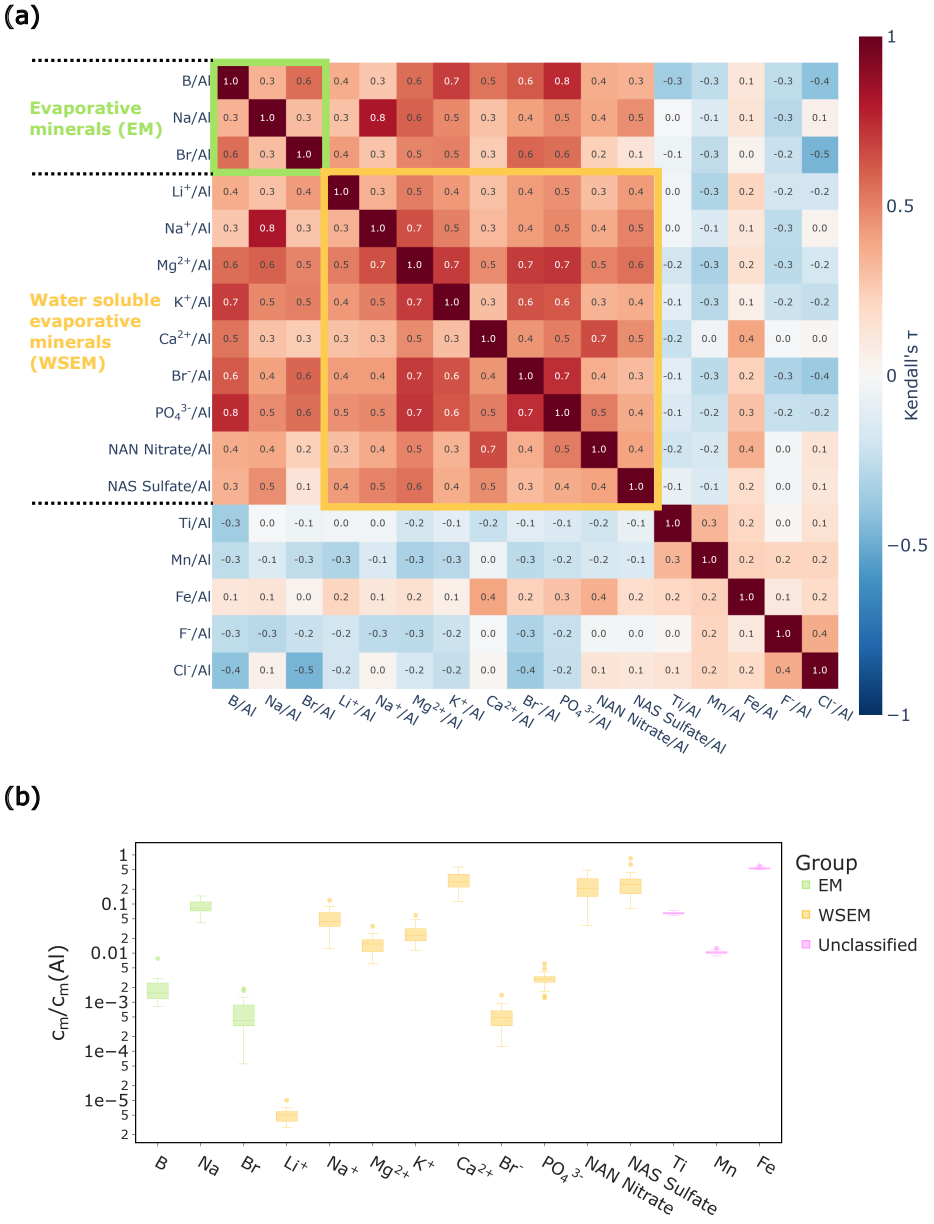


Figure S12. (a) Kendall's τ correlation coefficient matrix of Al-normalized mass concentrations of water-soluble ions and selected element groups over all analyzed *Dust* samples. (b) Box plots of Al-normalized mass concentrations of the according species for all analyzed *Dust* samples.

S9 Compositional heterogeneity of *Dust* driven by source regions and transport time

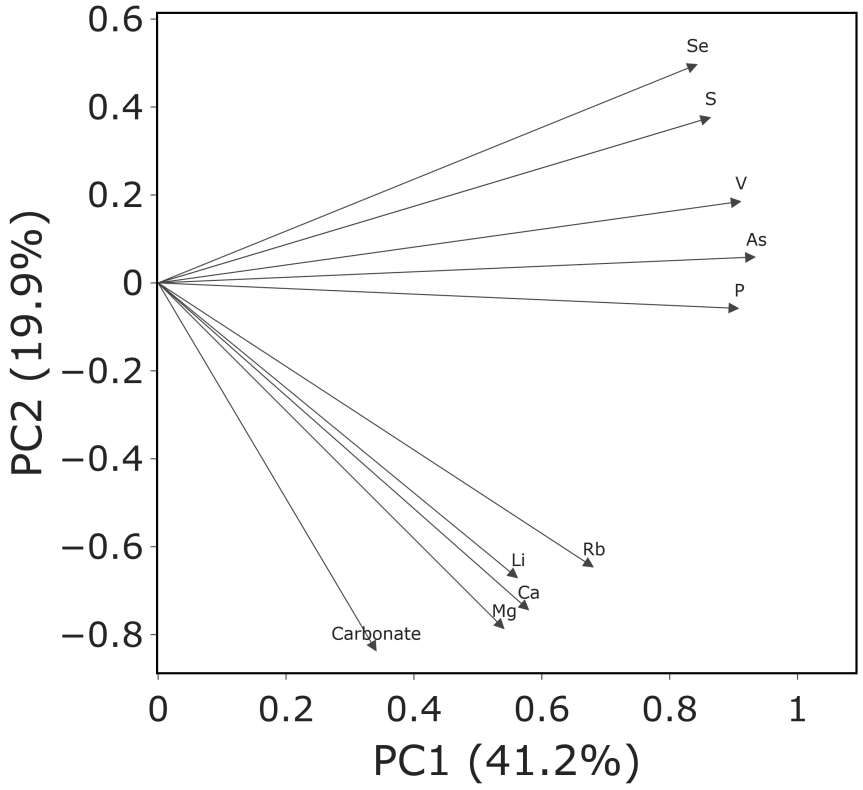


Figure S13. Principle component feature loadings plot of the principle component analysis (PCA) of Al-normalized element and ion mass concentrations, including all *Dust* samples with allocated source areas (event 25 was excluded as it strongly clusters as an outlier from all other samples). The five highest absolute loadings of each PC are displayed as arrows with species names attached. Standardized data of elements and ions with complete data coverage (above limit of detection) for all displayed *Dust* samples were included in the PCA.

S10 Statistical testing of *Dust* composition variability driven by source regions

Two-sided Mann–Whitney U tests were performed on data of unique dust plumes originating from the source areas PSA1 compared to PSA3 (cf. Fig. 1). For dust plumes, where multiple samples from consecutive arrival days at the JFJ were analyzed, mean Al-normalized composition data were calculated in order to assure independency of samples in the statistical testing. This lead to $n = 7$ unique dust plumes for PSA1 and $n = 14$ unique dust plumes for PSA3. Only elements and ions with data coverage for at least 6 unique plumes for PSA1 and 11 unique plumes for PSA3 were considered for testing.

Table S7. Mann–Whitney U test p-values for the comparison of Al-normalized mass concentrations of element and ion species observed in two different source areas: PSA1 ($n = 7$ unique plumes) vs. PSA3 ($n = 14$ unique plumes). Significant species are shaded in gray and marked by significance levels (***: $p < 0.001$, **: $p < 0.01$, *: $p < 0.05$).

Mass concentration ratio	**Mann–Whitney *U* test p-value (PSA1 vs. PSA3)**
CO_3^{2-}/Al	3.44e-05***
Mg/Al	6.88e-05***
Ca/Al	1.20e-04***
Cs/Al	3.27e-04***
Rb/Al	5.16e-04***
K/Al	7.74e-04***
Li/Al	0.00423**
Sr/Al	0.00745**
Ca^{2+}/Al	0.0159*
P/Al	0.0159*
As/Al	0.0379*
Pb/Al	0.0793
NAS/Al	0.0938
Sc/Al	0.110
NAN/Al	0.110
V/Al	0.128
Be/Al	0.149
Zr/Al	0.213
Ge/Al	0.216
S/Al	0.224
Cu/Al	0.255

Table S7. Continued.

Mass concentration ratio	Mann–Whitney *U* test p-value (PSA1 vs. PSA3)
F^-/Al	0.360
Mn/Al	0.360
Cl^-/Al	0.393
Ga/Al	0.488
K^+/Al	0.535
Ce/Al	0.535
Co/Al	0.535
Br/Al	0.536
La/Al	0.585
Ba/Al	0.588
Br^-/Al	0.636
Bi/Al	0.636
Li^+/Al	0.689
Fe/Al	0.689
Na/Al	0.743
Ti/Al	0.743
Se/Al	0.856
Sn/Al	0.856
PO_4^{3-}/Al	0.856
Mg^{2+}/Al	0.913
Cd/Al	0.971
Ho/Al	1.00
Sm/Al	1.00
Th/Al	1.00
Na^+/Al	1.00

S11 Statistical testing of *Dust* composition variability driven by transport time

Two-sided Mann–Whitney *U* tests were performed on data of unique dust plumes originating only from the source area PSA3 (cf. Fig. 1). For dust plumes, where multiple samples from consecutive arrival days at the JFJ were analyzed, mean Al-normalized composition data were calculated in order to assure independency of samples in the statistical testing.

Two transport time categories were defined as $0\,\mathrm{h}$ to $120\,\mathrm{h}$ and $120\,\mathrm{h}$ to $240\,\mathrm{h}$. Only elements and ions with full data coverage for at least 4 unique plumes for each transport time category were considered for testing.

Table S8. Mann–Whitney *U* test p-values for the comparison of Al-normalized mass concentrations of element and ion species observed in Saharan dust plumes from the source area PSA3 under two different transport time categories, from dust emission to sampling start at the JFJ: $0\,\mathrm{h}$ to $120\,\mathrm{h}$ ($n = 10$ unique plumes) vs. $120\,\mathrm{h}$ to $240\,\mathrm{h}$ ($n = 4$ unique plumes). Significant species are shaded in gray and marked by significance levels (***: $p < 0.001$, **: $p < 0.01$, *: $p < 0.05$).

Mass concentration ratio	**Mann–Whitney *U* test p-value (0–120 h vs. 120–240 h)**
Ho/Al	0.00404**
Tb/Al	0.00808**
Y/Al	0.0162*
Th/Al	0.0539
Cl^-/Al	0.0755
Sm/Al	0.0759
Se/Al	0.1059
Ti/Al	0.1059
Sn/Al	0.1059
Pb/Al	0.1059
Br^-/Al	0.1419
La/Al	0.1419
Cd/Al	0.1419
K^+/Al	0.1419
S/Al	0.1419
Li/Al	0.1878
Mg/Al	0.1878
Co/Al	0.2398

Table S8. Continued.

Mass concentration ratio	Mann–Whitney *U* test p-value (0–120 h vs. 120–240 h)
Br/Al	0.2601
Be/Al	0.3037
As/Al	0.3037
PO_4^{3-}/Al	0.3037
F^-/Al	0.3037
Mg^{2+}/Al	0.3037
Rb/Al	0.3736
P/Al	0.3736
Bi/Al	0.3736
V/Al	0.3736
CO_3^{2-}/Al	0.3736
Sr/Al	0.4535
Ca^{2+}/Al	0.6354
Na/Al	0.6354
Ca/Al	0.6354
Ga/Al	0.6354
Fe/Al	0.6354
Cu/Al	0.6354
Cs/Al	0.6354
Ce/Al	0.7333
Li^+/Al	0.8392
Na^+/Al	0.8392
Mn/Al	0.8392
Ba/Al	0.9399
K/Al	0.9451
Sc/Al	1.00

S12 Allocation of *Dust* composition variability to different Saharan dust plume source regions

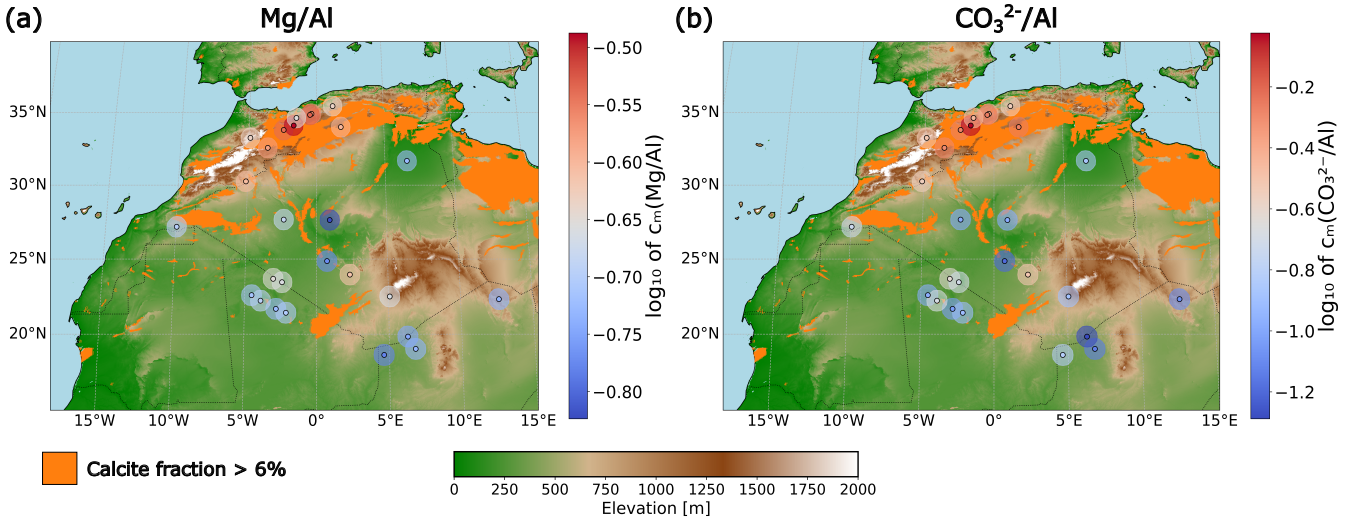


Figure S14. Physical maps showing Saharan dust plume source area centroids colored according to the corresponding log_{10} of Al-normalized mass concentrations of (a) CO_3^{2-} and (b) Mg measured at the JFJ. *Calcite* mineral contents of dust-productive soils are highlighted according to the *GMINER30* mineralogical database (Nickovic et al., 2012): Areas with clay size ($< 2\,\mu m$) top soil *calcite* content fractions above $6\,\%$ are shaded in orange.

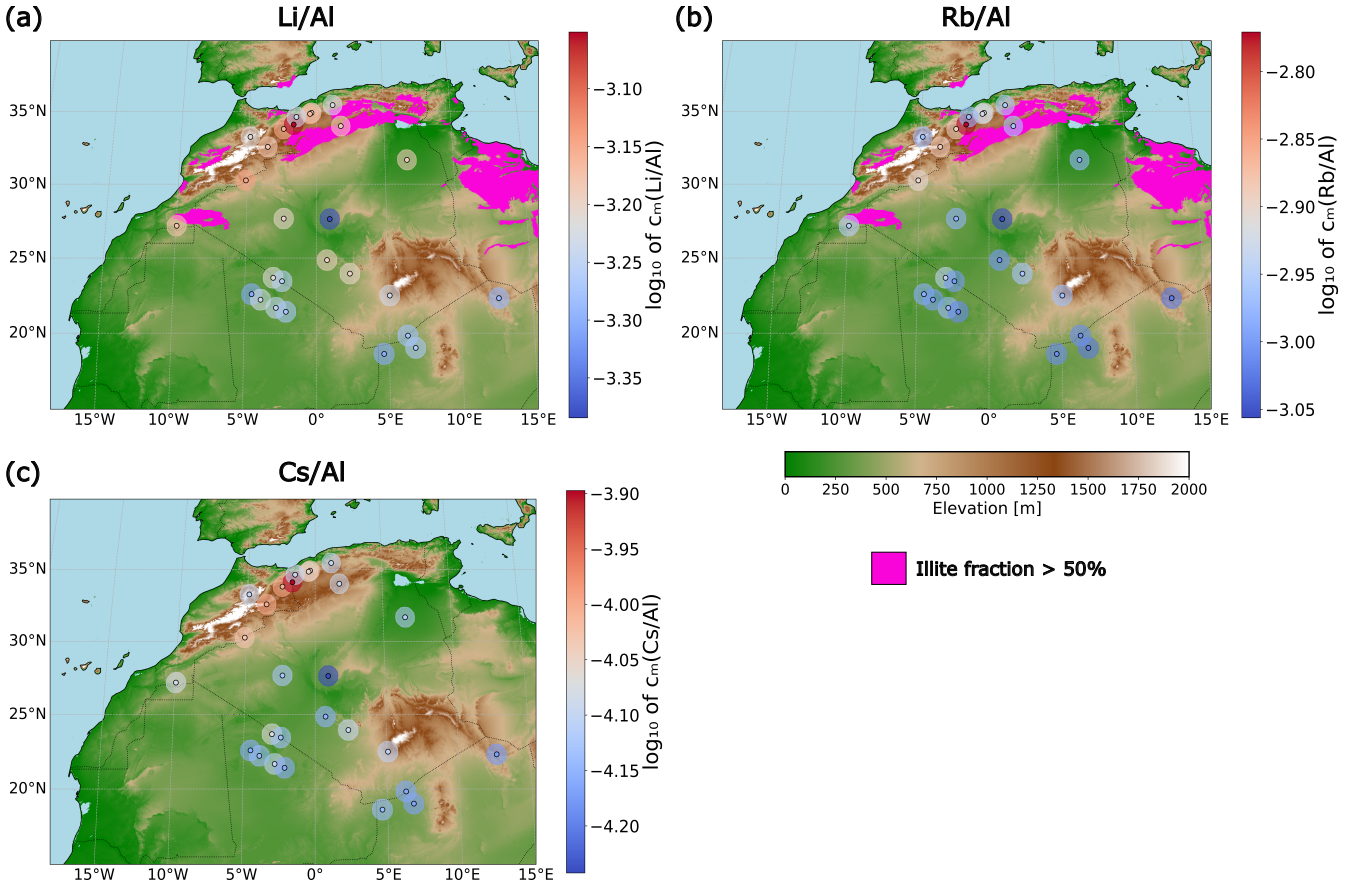


Figure S15. Physical maps showing Saharan dust plume source area centroids colored according to the corresponding log_{10} of Al-normalized mass concentrations of (a) Li, (b) Rb and (c) Cs measured at the JFJ. *Illite* mineral contents of dust-productive soils are highlighted according to the *GMINER30* mineralogical database (Nickovic et al., 2012): Areas with clay size ($< 2\,\mu m$) top soil *illite* content fractions above $50\,\%$ are shaded in pink.

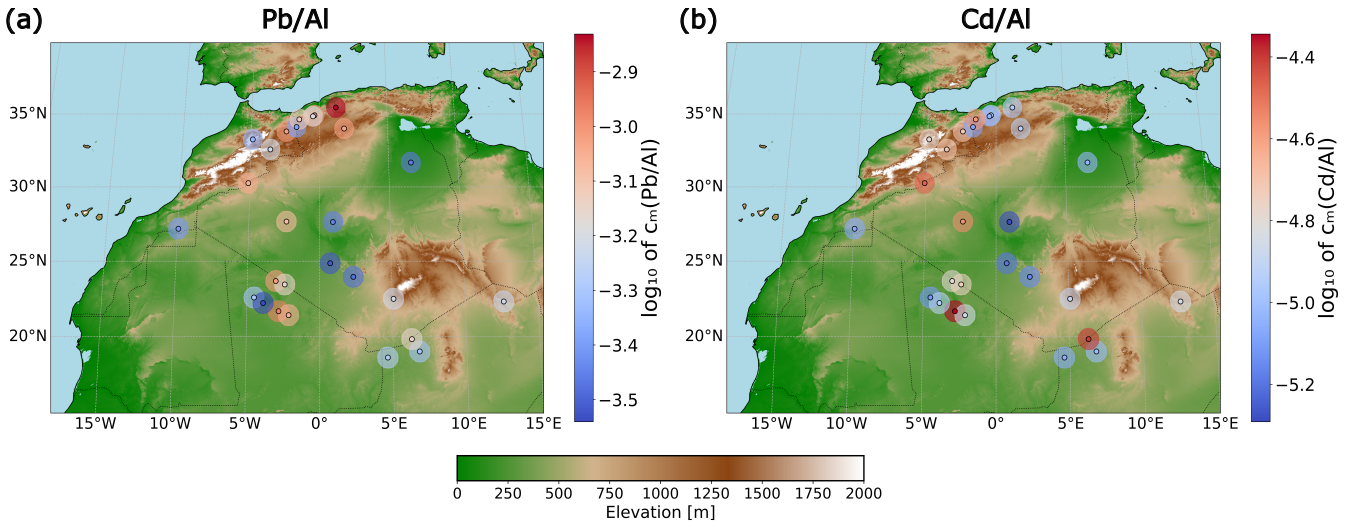


Figure S16. Physical maps showing Saharan dust plume source area centroids colored according to the corresponding log_{10} of Al-normalized mass concentrations of (a) Pb and (b) Cd measured at the JFJ.

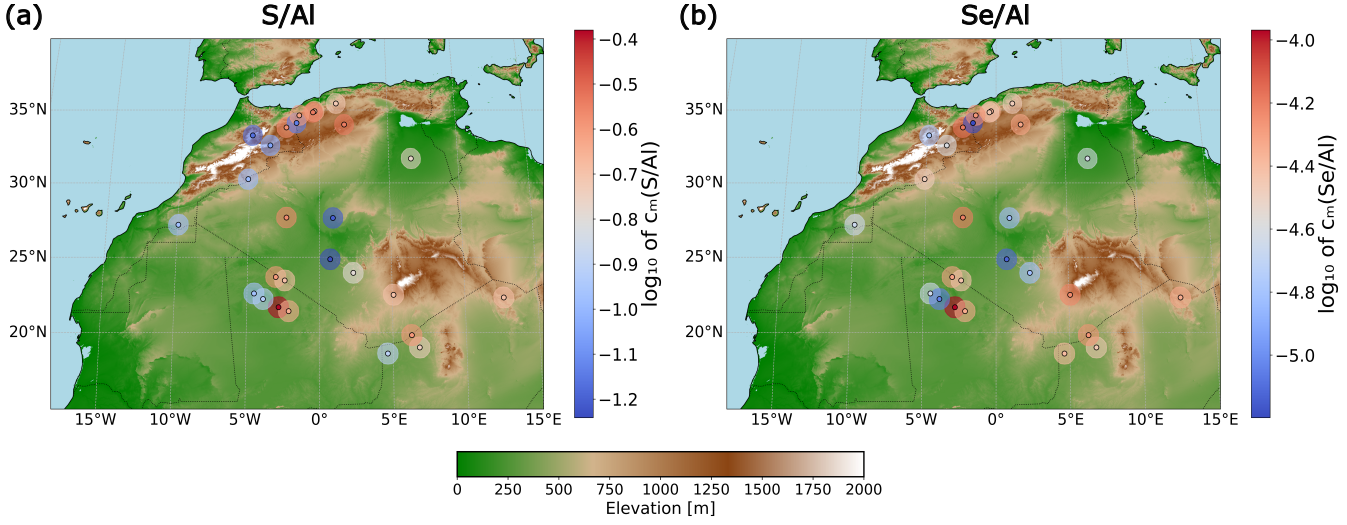


Figure S17. Physical maps showing Saharan dust plume source area centroids colored according to the corresponding log_{10} of Al-normalized mass concentrations of (a) S and (b) Se measured at the JFJ.

S13 Impact of transport time on *Dust* composition

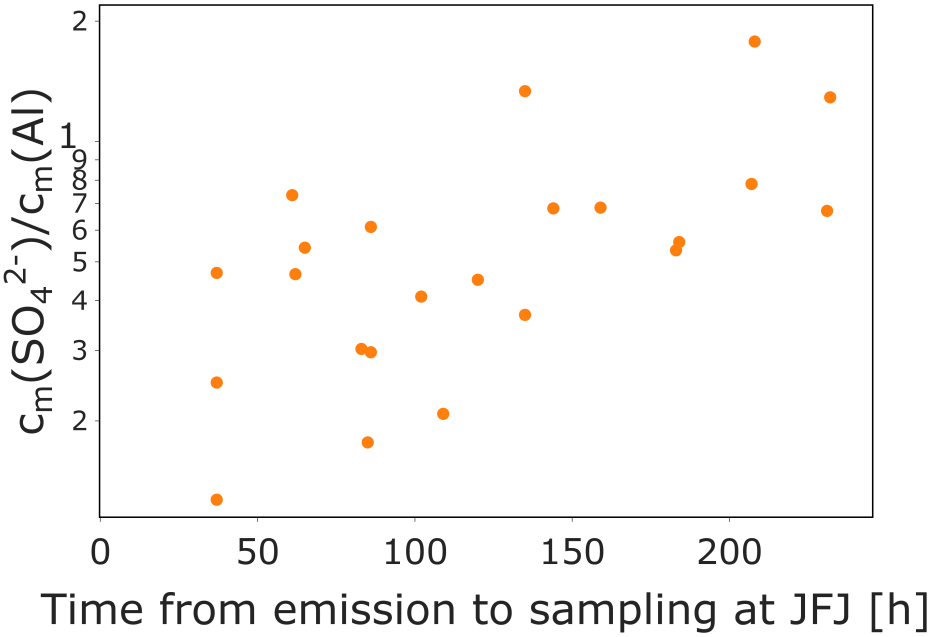


Figure S18. For Saharan dust plumes originating from PSA3, log_{10} Al-normalized mass concentrations of total sulfate as a function of dust plume transport time from emission to sampling start at the JFJ.

Table S9. Linear rates of change in Al-normalized element mass concentrations with transport time from dust emission to sampling at the JFJ for species exhibiting significant ($p < 0.05$) Kendall's τ correlations with transport time. Only samples from the source area PSA3 were included. Positive values indicate increasing ratios with transport time, while negative values indicate decreasing ratios. Rates are expressed per hour of transport time.

Mass concentration ratio	**Rate of change with transport time [h^{-1}]**
SO_4^{2-}/Al	3.89e-03
S/Al	1.50e-03
K^+/Al	2.26e-04
Mg^{2+}/Al	8.54e-05
B/Al	3.77e-05
Ti/Al	3.22e-05
PO_4^{3-}/Al	1.56e-05
Br/Al	5.36e-06
Pb/Al	3.28e-06
V/Al	2.59e-06
Sn/Al	5.49e-07
As/Al	4.85e-07
Se/Al	4.55e-07
Cd/Al	2.59e-07
Ho/Al	-3.63e-08
Tb/Al	-5.98e-08
Sm/Al	-1.64e-07
Th/Al	-2.04e-07
Y/Al	-1.01e-06

S14 Overview of instruments and methods applied in this study

Table S10. Overview of the online aerosol measurement instruments deployed at the JFJ, along with the corresponding derived analytical parameters utilized in this study; periods of data coverage used in this study are specified, accompanied by additional remarks where necessary.

Analytical parameter	**Instrument**	**Data coverage**	**Comment**
Aerosol absorption coefficients	AE-31 (Magee Scientific, Slovenia), AE-33 (Magee Scientific, Slovenia)	2011 to 2021	used for Saharan dust detection; $\lambda =$ 370 nm, 470 nm, 520 nm, 590 nm, 660 nm, 880 nm, 950 nm; AE-31 changed to AE-33 in 2015
Aerosol scattering coefficients	3563 (TSI, USA)	2011 to 2021	used for Saharan dust detection; $\lambda =$ 450 nm, 550 nm, 700 nm
Online $PM_{2.5}$ and PM_{10}	Fine dust monitor FIDAS 200 (PALAS, Germany)	October 2016 to 2021	Referenced to gravimetric PM_{10} standard method
Gravimetric PM_{10}	HiVol filters collection and weighing before and after collection with high precision analytical balance XP205 (Mettler Toledo, USA)	2011 to 2021	filter conditioning at 20 °C and 50 % RH for 96 h
NO_y (sum of reactive N-species)	Converter + CLD 89p (Eco Physics, Switzerland)	2011 to 02/2020	conversion to NO on heated gold surface (300 °C) (Zellweger et al., 2000)
CO	G2401 (Picarro, USA), APMA 360 and APMA 370 (Horiba, Japan)	2011 to 2021	AMPA changed to G2401 in 2012

Table S11. Overview of the offline HiVol filter based chemical parameters analyzed in this study, along with deployed instrumentation; periods of data coverage are specified, accompanied by additional remarks where necessary.

Analytical parameter	Instrument	Data coverage	Comment
Bulk OC, EC and carbonate mass concentration	Model 5 (Sunset Lab, USA), NIOSH protocol	*Dust* filter dates	
Bulk WSOC mass concentration	TOC-L-series (Shimadzu, Japan)	2011 to 2021 (4 day composites), *Dust* filter dates	Converted to WSOA by Offline-AMS OM/OC-ratios; excludes inorganic carbon by acidification (HCl, H_3PO_4) and sparging of water extracts before measurement (Cui et al., 2024)
Offline-AMS Bulk WSOC OM/OC-ratios	Aerosol Mass Spectrometer, Long Time-of-Flight (Aerodyne, USA)	2011 to 2021 (4 day composite)	cf. Weng et al. (2026)
Crustal elements and trace metals mass concentration	Inductively Coupled Plasma Mass Spectrometry (ICP-MS) iCAP TQ (Thermo Fisher Scientific, USA)	March 2019 to November 2019 (daily), *Dust* filter dates	full mineralization/digestion of filters
Inorganic anions and cations mass concentration	Ion Chromatography-Mass Spectrometry (IC-MS) with INTEGRION chromatography setup (Thermo Fisher Scientific, USA) and INTEGRION ISQ EC mass spectrometer (Thermo Fisher Scientific, USA)	2011 to 2021 (4 day composite)	

References

Caquineau, S., Gaudichet, A., Gomes, L., Magonthier, M.-C., and Chatenet, B.: Saharan dust: Clay ratio as a relevant tracer to assess the origin of soil-derived aerosols, Geophysical Research Letters, 25, 983–986, https://doi.org/10.1029/98GL00569, 1998.

Chow, J. C., Watson, J. G., Crow, D., Lowenthal, D. H., and Merrifield, T.: Comparison of IMPROVE and NIOSH Carbon Measurements, Aerosol Science and Technology, 34, 23–34, https://doi.org/10.1080/02786820119073, 2001.

Chow, J. C., Watson, J. G., Lowenthal, D. H., and Magliano, K. L.: Loss of $PM_{2.5}$ Nitrate from Filter Samples in Central California, Journal of the Air & Waste Management Association, 55, 1158–1168, https://doi.org/10.1080/10473289.2005.10464704, 2005.

Chow, J. C., Lowenthal, D. H., Chen, L.-W. A., Wang, X., and Watson, J. G.: Mass reconstruction methods for PM2.5: a review, Air Quality, Atmosphere & Health, 8, 243–263, https://doi.org/10.1007/s11869-015-0338-3, 2015.

Collaud Coen, M., Weingartner, E., Schaub, D., Hueglin, C., Corrigan, C., Henning, S., Schwikowski, M., and Baltensperger, U.: Saharan dust events at the Jungfraujoch: detection by wavelength dependence of the single scattering albedo and first climatology analysis, Atmospheric Chemistry and Physics, 4, 2465–2480, https://doi.org/10.5194/acp-4-2465-2004, 2004.

Collaud Coen, M., Brem, B. T., Gysel-Beer, M., Modini, R., Henne, S., Steinbacher, M., Putero, D., Gini, M. I., and Eleftheriadis, K.: Detection and climatology of Saharan dust frequency and mass at the Jungfraujoch (3580 m a.s.l., Switzerland), Atmospheric Chemistry and Physics, 26, 1623–1645, https://doi.org/10.5194/acp-26-1623-2026, 2026.

Cui, T., Manousakas, M. I., Wang, Q., Uzu, G., Hao, Y., Khare, P., Qi, L., Chen, Y., Han, Y., Slowik, J. G., Jaffrezo, J.-L., Cao, J., Prévôt, A. S. H., and Daellenbach, K. R.: Composition and Sources of Organic Aerosol in Two Megacities in Western China Using Complementary Mass Spectrometric and Statistical Techniques, ACS ES&T Air, 1, 1053–1065, https://doi.org/10.1021/acsestair.4c00051, 2024.

Fröhlich, R., Cubison, M. J., Slowik, J. G., Bukowiecki, N., Canonaco, F., Croteau, P. L., Gysel, M., Henne, S., Herrmann, E., Jayne, J. T., Steinbacher, M., Worsnop, D. R., Baltensperger, U., and Prévôt, A. S. H.: Fourteen months of on-line measurements of the non-refractory submicron aerosol at the Jungfraujoch (3580 m a.s.l.) – chemical composition, origins and organic aerosol sources, Atmospheric Chemistry and Physics, 15, 11 373–11 398, https://doi.org/10.5194/acp-15-11373-2015, 2015.

Herrmann, E., Weingartner, E., Henne, S., Vuilleumier, L., Bukowiecki, N., Steinbacher, M., Conen, F., Collaud Coen, M., Hammer, E., Jurányi, Z., Baltensperger, U., and Gysel, M.: Analysis of long-term aerosol size distribution data from Jungfraujoch with emphasis on free tropospheric conditions, cloud influence, and air mass transport, Journal of Geophysical Research: Atmospheres, 120, 9459–9480, https://doi.org/10.1002/2015JD023660, 2015.

Hueglin, C., Gehrig, R., Baltensperger, U., Gysel, M., Monn, C., and Vonmont, H.: Chemical characterisation of PM2.5, PM10 and coarse particles at urban, near-city and rural sites in Switzerland, Atmospheric Environment, 39, 637–651, https://doi.org/10.1016/j.atmosenv.2004.10.027, 2005.

Inness, A., Ades, M., Agustí-Panareda, A., Barré, J., Benedictow, A., Blechschmidt, A.-M., Dominguez, J. J., Engelen, R., Eskes, H., Flemming, J., Huijnen, V., Jones, L., Kipling, Z., Massart, S., Parrington, M., Peuch, V.-H., Razinger, M., Remy, S., Schulz, M., and Suttie, M.: The CAMS reanalysis of atmospheric composition, Atmospheric Chemistry and Physics, 19, 3515–3556, https://doi.org/10.5194/acp-19-3515-2019, 2019.

Jaffrezo, J.-L., Davidson, C. I., Kuhns, H. D., Bergin, M. H., Hillamo, R., Maenhaut, W., Kahl, J. W., and Harris, J. M.: Biomass burning signatures in the atmosphere of central Greenland, Journal of Geophysical Research: Atmospheres, 103, 31 067–31 078, https://doi.org/10.1029/98JD02241, 1998.

Knippertz, P. and Todd, M. C.: Mineral dust aerosols over the Sahara: Meteorological controls on emission and transport and implications for modeling, Reviews of Geophysics, 50, https://doi.org/10.1029/2011RG000362, 2012.

Nickovic, S., Vukovic, A., Vujadinovic, M., Djurdjevic, V., and Pejanovic, G.: Technical Note: High-resolution mineralogical database of dust-productive soils for atmospheric dust modeling, Atmospheric Chemistry and Physics, 12, 845–855, https://doi.org/10.5194/acp-12-845-2012, 2012.

Rodríguez, S., Alastuey, A., Alonso-Pérez, S., Querol, X., Cuevas, E., Abreu-Afonso, J., Viana, M., Pérez, N., Pandolfi, M., and de la Rosa, J.: Transport of desert dust mixed with North African industrial pollutants in the subtropical Saharan Air Layer, Atmospheric Chemistry and Physics, 11, 6663–6685, https://doi.org/10.5194/acp-11-6663-2011, 2011.

Schmetz, J., Pili, P., Tjemkes, S., Just, D., Kerkmann, J., Rota, S., and Ratier, A.: AN INTRODUCTION TO METEOSAT SECOND GENERATION (MSG), Bulletin of the American Meteorological Society, 83, 977–992, https://doi.org/10.1175/1520-0477(2002)083<0977:AITMSG>2.3.CO;2, 2002.

Usher, C. R., Michel, A. E., and Grassian, V. H.: Reactions on Mineral Dust, Chemical Reviews, 103, 4883–4940, https://doi.org/10.1021/cr020657y, 2003.

Waked, A., Favez, O., Alleman, L. Y., Piot, C., Petit, J.-E., Delaunay, T., Verlinden, E., Golly, B., Besombes, J.-L., Jaffrezo, J.-L., and Leoz-Garziandia, E.: Source apportionment of PM_{10} in a north-western Europe regional urban background site (Lens, France) using positive matrix factorization and including primary biogenic emissions, Atmospheric Chemistry and Physics, 14, 3325–3346, https://doi.org/10.5194/acp-14-3325-2014, 2014.

Weng, J., Hao, Y., Brem, B. T., Cui, T., Khare, P., Dada, L., Daellenbach, K. R., Darfeuil, S., Uzu, G., Jaffrezo, J.-L., Steinbacher, M., Reimann, S., Gkraikou, T., Oikonomou, K., Sciare, J., Collaud Coen, M., Mohr, C., Prévôt, A. S. H., Gysel-Beer, M., El Haddad, I., and Winiger, P.: A Decadal-Scale Perspective on PM10 Composition and its Variability Drivers at the Alpine High-Altitude Research Station Jungfraujoch, EGUsphere, pp. 1–31, https://doi.org/10.5194/egusphere-2026-3660, 2026.

White, W. M.: Geochemistry, Wiley, Hoboken, NJ, second edition edn., ISBN 978-1-119-43805-2, 2020.

Yan, C., Nishida, J., Yuan, R., and Fayer, M. D.: Water of Hydration Dynamics in Minerals Gypsum and Bassanite: Ultrafast 2D IR Spectroscopy of Rocks, Journal of the American Chemical Society, 138, 9694–9703, https://doi.org/10.1021/jacs.6b05589, 2016.

Zellweger, C., Ammann, M., Hofer, P., and Baltensperger, U.: NOy speciation with a combined wet effluent diffusion denuder – aerosol collector coupled to ion chromatography, Atmospheric Environment, 33, 1131–1140, https://doi.org/10.1016/S1352-2310(98)00295-7, 1999.

Zellweger, C., Ammann, M., Buchmann, B., Hofer, P., Lugauer, M., Rüttimann, R., Streit, N., Weingartner, E., and Baltensperger, U.: Summertime NOy speciation at the Jungfraujoch, 3580 m above sea level, Switzerland, Journal of Geophysical Research: Atmospheres, 105, 6655–6667, https://doi.org/10.1029/1999JD901126, 2000.